Computational Investigation of Effects of Expanded Metal Foils on the Lightning Protection Performance of a Composite Rotor Blade

Yong Seong Kang[1] · Se Woong Park[1] · Jin Su Roh[2]· Rho Shin Myong[1]

[1] School of Mechanical and Aerospace Engineering, Gyeongsang National University, Jinju, South Korea

[2] Aircraft Certification Department, Korea Institute of Aviation Safety Technology, Incheon, South Korea

Abstract

Lightning is one of the most important threats to the safe operation of an aircraft. Rotorcraft can experience lightning strikes on the main rotor blades and tail rotor blades which can seriously affect the rotorcraft and its components in several ways. When lightning strikes a rotor blade made of composite material, electrical-thermal multi-physical phenomena such as the Joule heating effect occur. In this study, an electrical-thermal computational simulation of lightning strikes on composite rotor blades was performed. The simulation analyzed various situations including the presence of a lightning protection system on the composite rotor blade. Emphasis was placed on the effects of geometric parameters of expanded metal foil on the lightning protection performance. In addition, the effects of curvature on thermal and electrical response were investigated. The thermally damaged area was found to substantially increase in inner layers compared to the flat plate case.

Keywords: Lightning Protection System, Composite, Rotor Blade, Coupled Electrical-Thermal, Expanded Metal Foil

1. Introduction

Aircraft can experience various harsh environments during flight, such as a lightning strike, which

[1] Corresponding Author: R. S. Myong, myong@gnu.ac.kr

can have catastrophic consequences. Lightning striking an aircraft can produce both direct and indirect effects [1]. The direct effects are physical damage, such as melting, drilling, and deformation, of the exterior skin or the structure of an aircraft [2]. The indirect effects involve transient phenomenon resulting from the induction of a strong electromagnetic field in the electronic equipment of the aircraft, resulting in severe operational disruptions. Most lightning strikes on an aircraft are triggered by the aircraft itself, rather than being struck by a lightning strike between a thundercloud and the ground [1,3-6]. The principle of triggered lightning is that the aircraft accumulates an electric charge from the atmosphere during flight and emits energy instantaneously when it encounters a thundercloud with a high density of electric charge, thus triggering lightning from the aircraft [3].

Rotorcrafts frequently cause triggered lightning because they characteristically fly at a relatively low speed and at low altitude, unlike fixed-wing aircraft. Most of the lightning strikes on rotorcraft occur on the rotor blades (main and tail) [4,7]. When lightning strikes the rotor blade of a rotorcraft, it causes direct lightning effects, that is, physical damage to the rotor blade [8,9]. Severe physical damage to the main or tail rotor blades can lead to accidents, such as the loss of rotorcraft maneuverability. Studying the direct effects of lightning strikes on the rotor blades of rotorcraft is therefore essential to the design of lightning protection systems (LPS) and ensuring the safe operation of rotorcraft.

Various types of LPS were developed to protect composites from lightning strikes. They include woven fabric with metal wire, expanded metal foil, and composite fibers coated with conductive materials [10,11-12]. However, expanded metal foil (EMF) is still the most effective because it has many advantages related to high electrical conductivity, manufacturing process and airworthiness certification [13,14]. Guo *et al.* [15] reported recently that expanded foils with the anisotropic electrical conductivity can enhance the performance of lightning strike protection of carbon fiber composites. Guo *et al.* [16] also reported that the inherent electrically insulating, thermally insulating and refractory properties of fiberglass make it possible to construct an isolation layer that suppresses the downward penetration of lightning electric and heat into the underlying CFRP. Wang *et al*. [17] conducted a study on the design parameters such as width and material of EMF on the lightning

protection performance.

Previous studies [18-21] have conducted electrical-thermal coupled multiphysics analyses of the effects of lightning for a given condition defined in the guideline. Hu *et al.* [14] conducted a fully-coupled simulation of electrical, thermal, and structure and compared the simulation results with the experimental data. Several electrical-thermal-structural simulations [22,23] were also conducted in the past three years. In addition, several studies have investigated the effect of lightning on joule heating as well as arc heating [24-27]. Considering joule heating and arc heating at the same time can improve the accuracy of the simulation because it is closer to the actual lightning phenomenon.

Further, several studies [28-30] considered the effect of pressure loading on shock waves caused by lightning strikes. Recent simulation methods not only take into account the electrical-thermal effect, but also predict structural damage, thereby improving the prediction accuracy of the damaged area due to lightning strikes. Table 1 summarizes the previous simulation studies using various codes like ABAQUS, ANSYS, COMSOL, and CST Studio. It includes the results of recent years of research on computational simulation techniques and lightning protection devices. It can be noted that most of previous computational simulations were limited to the flat plate specimen and no electrical-thermal computational simulation was conducted on the curved specimen.

The rotor blades of rotorcrafts were mainly composed of a composite material. For this reason, the previous studies investigated the damaged area of the general composite structure considering the thermal effects caused by the lightning's current. Studies on the effects of lightning strikes on aircraft, for both simulated and analytical investigations, start with the conditions defined in the SAE Series document, the aircraft lightning certification guideline [6,18-19].

In this study, a multiphysics approach was used to perform a computational simulation of the direct effects of a lightning strike on a composite rotor blade. The electrical-thermal coupled model with a dominant effect on the failure area of the composite and lightning protection devices was considered. In addition, it was judged that the tendency of the damaged area according to the geometric design parameters could be investigated through an electrical-thermal coupled simulation method. The present study may be considered the first attempt to systematically investigate the effects of geometric

parameters of expanded metal foil on the lightning protection performance, including the long way of diamond, short way of diamond, strand width, and thickness. In addition, we investigate the effects of curvature on thermal and electrical response, which are essential in the study of complicated geometries like a rotor blade.

We first briefly explain lightning certification issue and lightning zones and waveforms in Sections 2 and 3. We then describe theoretical background for the coupled electrical-thermal analysis in Section 4. The computational simulation model of the composite rotor blade is defined in Section 5. The comparative computational analysis of the lightning effects with and without installation of the LPS on the rotorcraft is presented in Section 6. Also, the ablation rate of the LPS is analyzed for different temperatures and the performance of the LPS is evaluated for varying geometrical parameters. Lastly, for the curved composite material, the electrical-thermal coupled effects according to various curvatures are investigated.

Table 1. Review of literature on computational simulation of the direct effects of lightning strikes on composite material

References	**Physical Modeling**	**Geometric Model**	**Analysis Tools**	**Application of LPS**
Nunes de Souza (2007) [32]	Electrical	Flat Plate Specimen, Wing Box Structure	CST Studio Suite	Metallic Strips
Espejel *et al*. (2017) [33]	Electrical-Thermal	Flat Plate Specimen	ABAQUS	Copper EMF, Carbon Nano Tube
Wang *et al*. (2018) [22]	Electrical-Thermal-Structural	Flat Plate Specimen	ANSYS	No LPS
Xiao *et al*. (2018) [28]	Electrical-Thermal, Pressure Loading	Flat Plate Specimen	ABAQUS	No LPS
Karch *et al*. (2018) [30]	Electrical-Thermal, Pressure Loading	Flat Plate Specimen	ANSYS	Copper EMF
Chen *et al*. (2018) [23]	Electrical-Thermal-Structural (Lightning Arc)	Flat Plate Specimen	ANSYS, ABAQUS	No LPS
Foster *et al*. (2019) [29]	Electrical-Thermal, Pressure Loading	Flat Plate Specimen	ABAQUS	No LPS
Wang *et al*. (2019) [17]	Electrical-Thermal	Flat Plate Specimen	ABAQYS, ANSYS	Copper EMF (Basic Parametric Study)
Wan *et al*. (2019) [25]	Electrical-Thermal, Lightning Arc	Flat Plate Specimen	ABAQUS	No LPS

Zhang *et al*. (2019) [11]	Electrical-Thermal	Flat Plate Specimen	ABAQUS	Silver Coating, Carbon Nano Tube Film
Millen *et al*. (2019) [27]	Electrical-Thermal, Lightning Arc	Flat Plate Specimen	ABAQUS, COMSOL	Copper EMF
Millen *et al*. (2019) [31]	Electrical-Thermal, Pressure Loading	Flat Plate Specimen	ABAQUS	No LPS
Hu *et al*. (2019) [14]	Electrical-Thermal-Structural	Flat Plate Specimen	ABAQUS	Copper EMF
Present	Electrical-Thermal	Flat Plate and Curved Specimen	ABAQUS	Copper EMF (Wider Geometric Parametric Study)

2. Outline of Lightning Certification

Aircraft must satisfy the requirements specified by the certification authority in order to operate in any air space. Because lightning can lead to catastrophic consequences during flight, it is a critical factor in airworthiness certification. Even if the aircraft is struck by lightning during flight, it must be able to not only continue to fly but also land safely [6,8,19]. Aircraft certification documents for lightning include various regulations and guidance; the Code of Federal Regulations (CFR) and Advisory Circular (AC) regulated by the Federal Aviation Administration (FAA), whose detailed information on lightning certification is contained in ARP series documents issued by the SAE, and in the DO-160 issued by the Radio Technical Commission for Aeronautics (RTCA). SAE ARP 5577 provides detailed guidance related to the direct effects of lightning strikes on aircraft.

The regulations for rotorcraft certification for lightning strikes are provided separately in AC 27-1B and AC 29-2C. According to these documents, the rotor blades and rotor transmissions are the main structures that must be protected against any catastrophic damage resulting from the direct effects of lightning strikes on a rotorcraft.

3. Simulation of Lightning Strike

3.1 Lightning Zoning

SAE ARP 5414 specifies zones which indicate the location of the lightning strike on the aircraft. Not all aircraft are exposed to the same lightning environment, because the lightning characteristics of

aircraft can differ depending on the type and shape of the aircraft. Therefore, the lightning zone reflects the lightning strike characteristics at each point of the aircraft. The lightning zone is divided into 1, 2, and 3 depending on the initial impact, and is divided into 6 zones according to detailed characteristics [6]. The general lightning zones of aircraft provided by SAE ARP can be divided into the following:

- Zone 1A: First Return Stroke Zone
- Zone 1B: First Return Stroke Zone with Long Hang-On
- Zone 1C: Transition Zone for First Return Stroke
- Zone 2A: Swept Stroke Zone
- Zone 2B: Swept Stroke Zone with Long Hang-On
- Zone 3: Current Conduction Zone

Rotorcraft has different lightning zone characteristics compared to fixed-wing aircraft, due to the effects of hovering flight, and rotor blades [4]. The external elements except the rotor blade should be treated as zone 1B. The attachment of a swept channel may occur anywhere from zone 1B, and hence the remaining part not defined as zone 1B, the lower fuselage, should be considered zone 1A. Since the tip part of the rotor blade can induce the attachment of the initial leader, a point within 0.5m of the tip of the rotor blade is considered to be zone 1A [34]. The remaining area except for zone 1A on the rotor blade is considered to belong to zone 2A. The area on the upper fuselage protected by the rotating main rotor blades is treated as zone 3. The definition of the zone depends on the type of tail rotor. An example of these lightning strike zones is shown in Figure 1.

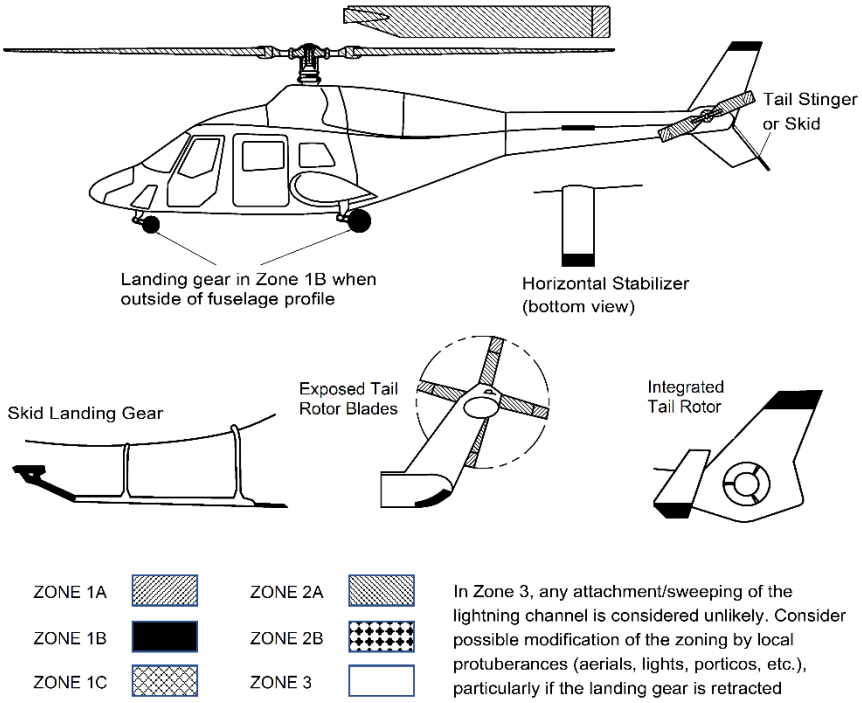

Figure 1. Example of lightning strike zones for rotorcraft

3.2 Lightning Simulated Waveform

SAE ARP 5412 provides guidance on simulating lightning. Depending on the lightning strike environment of the aircraft, various lightning waveform combinations are used. The standard current waveforms of simulated lightning, as defined in the SAE ARP guidance, consist of A, B, C, D, and H waveforms [6]. The simulated waveform of standard current used to evaluate the direct effects of aircraft lightning is shown in Fig. 2. The current waveforms for each component are shown in Fig. 3 (a) to (d). All waveforms are based in the time domain, not the frequency domain [6,18,35].

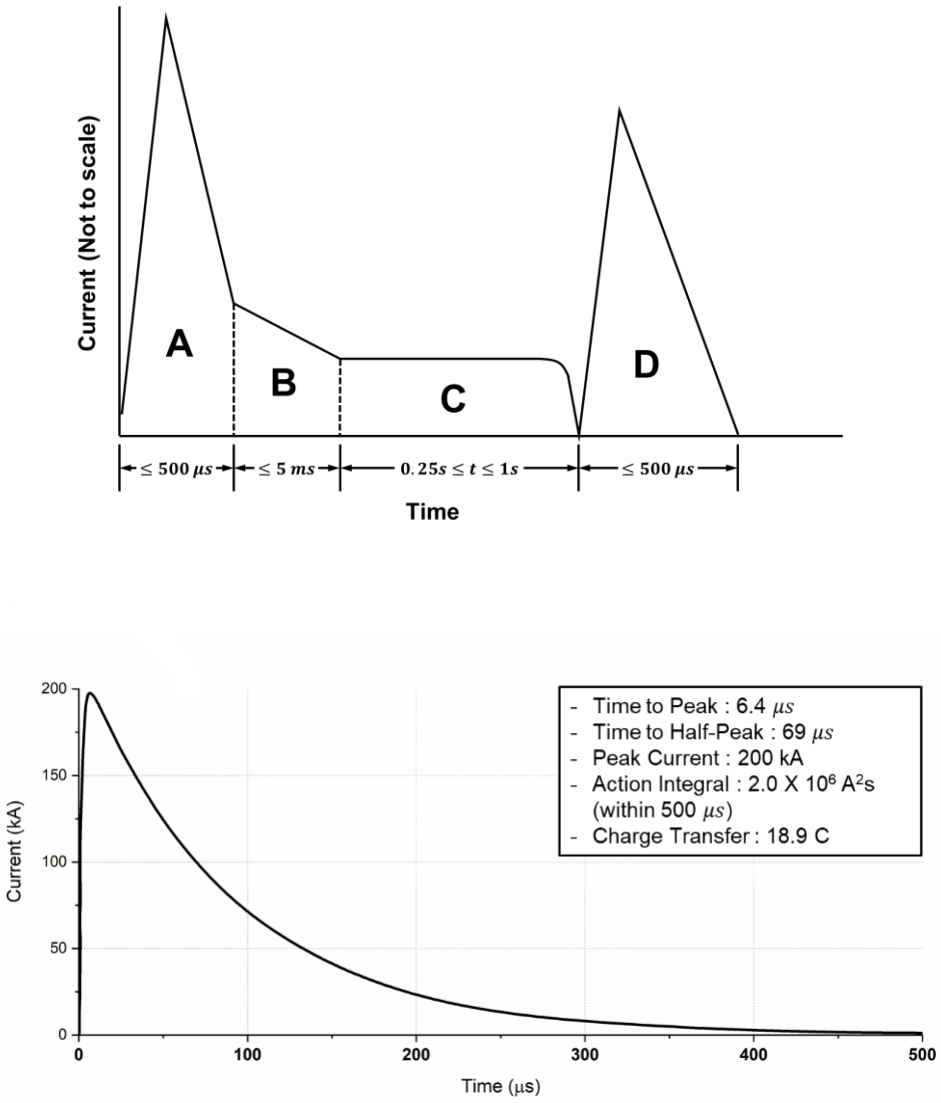

Figure 2. Idealized standard current waveform and current waveform A

The following double exponential function can mathematically represent the waveforms of all lightning strikes;

$$I(t) = I_0(e^{-\alpha} - e^{-\beta t})(1 - e^{-\gamma t})^2 \quad (1)$$

The values of the parameters in Eq. (1) are summarized in Table 2. The waveform current component A simulates the first return stroke, which can vary with the flight altitude of the aircraft. Waveform A has a duration of less than 500 μs. It also has the highest peak current value among all the waveform current components. Because of the enormous energy injected in a short period, it can cause explosive damage. In particular, it is possible to cause de-lamination damage if the epoxy in the carbon fiber

composite material evaporates.

Table 2. Values of parameters in mathematical expression of idealized lightning current component

Parameter	Lightning Current Component			
	A	B	C	D
I_0 (A)	218,810	11,300	400	109,405
α (s^{-1})	11,354	700	N/A	22,708
β (s^{-1})	647,265	2,000	N/A	1,294,530
γ (s^{-1})	5,423,540	22,000	N/A	10,847,100

Table 3 summarizes the current component combinations for the application of rotorcraft zoning for lightning strikes as defined in Section 3.1.

Table 3. Application of lightning environment to aircraft zones

Aircraft Zone	Current Components
1A	A, B, C*, H
1B	A, B, C, D, H
1C	A_H, B, C*, D, H
2A	D, B, C*, H
2B	D, B, C, H
3[a]	A, B, C, D, H
3[b]	A/5, B, C*

a. Conducted Area
b. Direct Attachment Lightning Environment for Zone 3 External Surface

4. Theoretical Background of Computational Analysis

Recently, because of the increasing availability of computing resources and software, research on the computational simulation of lightning strikes on aircraft is increasingly being conducted. In particular, the accuracy and reliability of lightning computational simulations have significantly improved due to increased validation using actual experimental data. Computational simulations are typically used to predict qualitative trends and identify potential design defects. They can also provide corrective actions in advance when designing a lightning protection system, serving as an aid to actual testing and reducing time and cost.

In this study, computational simulations of the effects of lightning strikes were carried out using ABAQUS software, which was developed based on the finite element method (FEM), and is suitable for implementing anisotropic structures such as composite rotor blades. ABAQUS can also handle multi-physical problems that arise in lightning, by using coupled electrical and thermal elements [17-19].

4.1 Joule Heating Effect

Joule heating, also known as Ohmic heating or resistive heating, is defined as the amount of heat generated when a current passes through a resistor. Joule heating can be written as,

$$P_{ec} = E \cdot J = E \cdot \sigma^{E} \cdot E \tag{2}$$

where P_{ec} is the electrical energy lost by the current through the conductor, in other words, the amount of change from electrical energy to thermal energy. E is the electrical field intensity, J is the current density per unit area, and σ^{E} is the electrical conductivity. Electrical conductivity has a reciprocal relationship with the electrical resistance. The amount of heat generated by the Joule heating effect is greatly affected by electrical resistance. Also, as the temperature of the conductor increases, the electrical conductivity generally decreases. An increase in electrical resistance leads to an increase in the amount of heat. Therefore, when conducting a lightning simulation, both thermal and electrical aspects should be considered simultaneously.

4.2 Coupled Thermal-electrical Analysis

The conservation of charge equation, after assuming a steady-state state, is given by [36]:

$$\int_{S} J \cdot n dS = \int_{V} r_c dV \tag{3}$$

where V and S are the unit volume and area, respectively, n is the outward normal to S, and r_c is the internal volumetric current source per unit volume.

According to Ohm's law, the current density J can be described as follows,

$$J = \sigma^{E} \cdot E = -\sigma E \cdot \frac{\partial \varphi}{\partial x} \tag{4}$$

where the field intensity $E(x)$ is defined as the negative gradient of the potential. φ is a potential, and σ is the electrical conductivity. $\sigma^{E}(\theta, f^{\alpha})$ is defined as a matrix comprised of the temperature θ and a variable field f^{α}.

Using Eqs. (3), (4), the governing equations for the finite element method can be obtained as follows,

$$\int_{V} \frac{\partial \delta \varphi}{\partial x} \cdot \sigma^{E} \cdot \frac{\partial \varphi}{\partial x} dV = \int_{S} \delta \varphi J dS + \int_{V} \delta \varphi r_c dV \tag{5}$$

The energy conservation equation of heat flow can be expressed as follows,

$$\int_V \rho c \frac{\partial \theta}{\partial t} \cdot \delta\theta dV + \int_V \frac{\partial \delta\theta}{\partial x} \cdot k \cdot \frac{\partial \theta}{\partial x} dV = \int_V \delta\theta r dV + \int_S \delta\theta q dS \tag{6}$$

where ρ is the density of the media, c is the specific heat, k is the coefficient of the thermal conductivity, q is the heat flux per unit area, and r is the heat generated inside the object.

The spatial discretization of the governing equations for the electric and thermal energy on individual nodes using Newton's method provides a mathematical form, expressed in the asymmetric Jacobian matrix [18]:

$$\begin{bmatrix} K_{\varphi\varphi} & K_{\varphi\theta} \\ K_{\theta\varphi} & K_{\theta\theta} \end{bmatrix} \begin{bmatrix} \Delta\varphi \\ \Delta\theta \end{bmatrix} = \begin{bmatrix} R_{\varphi} \\ R_{\theta} \end{bmatrix} \tag{7}$$

where K_{ij} is a partial matrix of a fully coupled Jacobian, $\Delta\varphi$ and $\Delta\theta$ are the electrical potential and temperature increments, respectively, and R_{φ} and R_{θ} are electrical and thermal residual vectors, respectively.

The fully coupled thermal-electrical equation simultaneously calculates the temperature and electrical potential at each node. The present method considers the heat transfer associated with the interaction of surface radiation for the spatial radiation of a three-dimensional model but ignores convection effects [17,19].

The computational simulation using the coupled thermal-electrical analysis module of ABAQUS has been validated for general composites in previous studies [17,18]. Ogasawara *et al*. [17] and Ranjith *et al*. [18] compared the computational results with lightning test data for composite specimens. The composites used in the study consisted of 32-ply, and the fibers were laminated with a quasi-isotropic $[45°/0°/-45°/\ 90°]_{4S}$ pattern. It was found that the area of critical temperature where the composite was delaminated and the area of high temperature due to Joule heating are qualitatively similar to the experimental results [6] obtained with an ultrasonic C-Scan of the delaminated area. Therefore, the coupled thermal-electrical analysis module of ABAQUS can be carried over to the analysis of the lightning effects on rotor blades of rotorcraft made of composite materials.

5. Computational Simulation Model

5.1 Cross-Sectional Geometry of the Rotor Blade

The main rotor blade of the UH-60 helicopter was selected as the configuration for the computational simulation. As shown in Fig. 3, the rotor blade of a UH-60 helicopter has a box spar type structure [37-39]. The main structural elements of the spar are the upper spar cap and lower spar cap, which are located on the top and the bottom of the spar. Both spar caps withstand the load of the rotor blade, while the two spar webs (main and aux) withstand the longitudinal shear stress. The initial lightning impact on the structural elements of the rotor blade spar is generally assumed to occur on the upper spar cap.

Figure 4 provides the laminated pattern for the upper spar cap. The upper spar cap is made of quasi-isotropic lamination [90°/-45°/45°/0°] using a unidirectional carbon composite material [37,39]. The computational simulation was performed as a coupon test. It describes the laminated pattern on the upper spar cap and is an appropriate method of evaluating the direct effects of lightning, which cause physical damage. The effect of paint applied to the surface of the rotor blade was not considered in the present study. The geometry and boundary conditions of the specimen used for the coupon test will be detailed in Section 5.3.

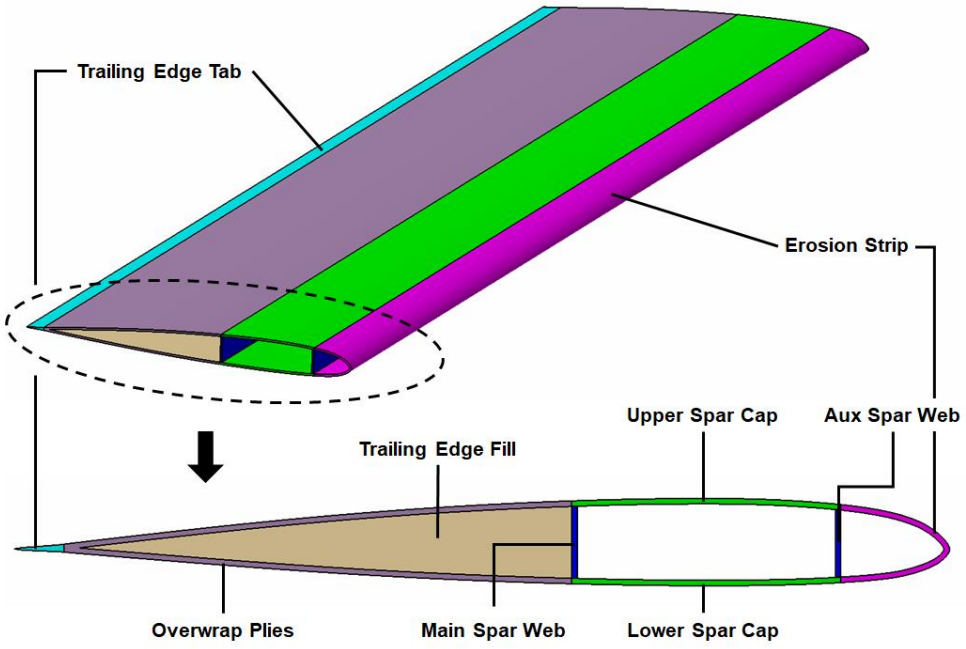

Figure 3. Structure of the main rotor blade of UH-60 helicopter [37,38]

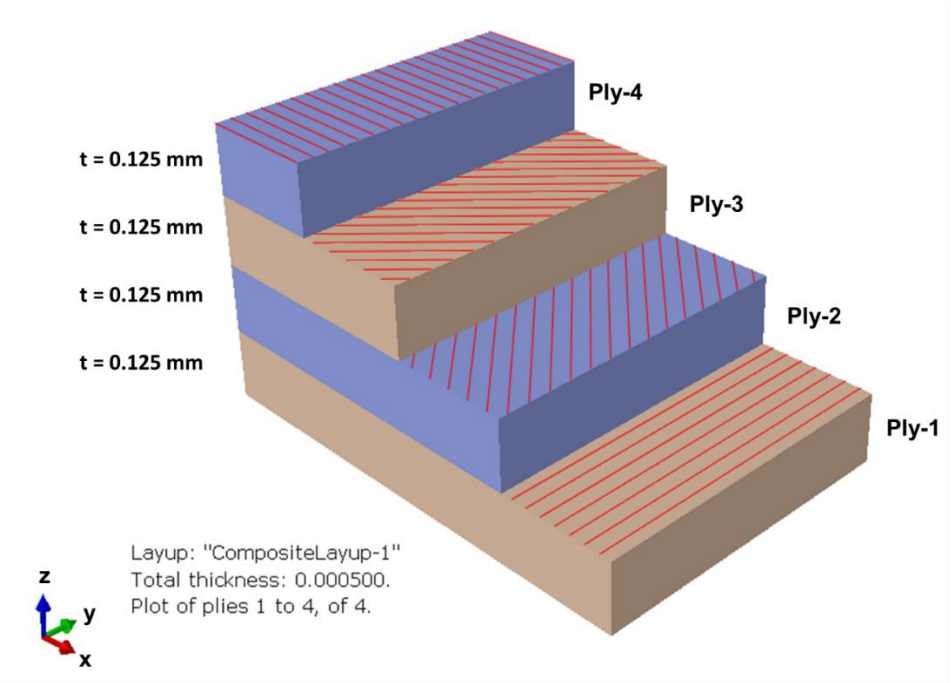

Figure 4. CFRP laminate model of upper spar cap of the rotor blade

5.2 Properties of the Materials

Several studies have been conducted, including Ogasawara *et al*. [17], to predict the effects and damages caused by lightning strikes on carbon fiber-reinforced plastics (CFRP). CFRP has different physical (thermal and electrical) properties depending on the longitudinal, transverse, and thickness direction of the fiber. CFRP contains epoxy resins, which are highly susceptible to thermal energy. Damage to epoxy resins can lead to structural degradation and damage, and can eventually result in rotorcraft accidents [40]. Therefore, the CFRP properties should be handled in a careful manner to ensure accurate understanding of the temperature effects in a fully coupled thermal-electrical analysis. In the study conducted by Ogasawara *et al*., the thermal and electrical properties of an IM600 / 133 (fiber/epoxy) CFRP were assumed to change linearly with temperature. Another study, conducted by Lee *et al*. [19], used the properties of an AS4 /3506a CFRP, which were experimentally measured to obtain more accurate results.

In the present analysis of the effects of lightning strikes, a composite made up of AS4 fiber and 3506a epoxy similar to the one used by Lee *et al*. was employed in the laminate pattern of the rotor blade. The properties of AS4/3506a CFRP are comparable to those of the IM600/133 used in

Ogasawara *et al*.'s work. The AS4/3506 CFRP properties at various temperatures are summarized in Table 4.

Table 4. Steady-state temperature-dependent properties of CFRP AS4/3506a [19]

Temp. T (K)	Density, ρ (kg/m^3)	Specific Heat C_p (J/kg · K)	Thermal Conductivity			Electrical Conductivity		
			Long. k_{11} (W/m·K)	Trans. k_{22} (W/m·K)	Thick. k_{33} (W/m·K)	Long. σ_{11} (S/m)	Trans. σ_{22} (S/m)	Thick. σ_{33} (S/m)
298	1520	1065	46.60	0.6830	0.6830	35970	1.1500	0.0039
623	1520	2100	24.70	0.3730	0.3730	35970	1.1500	0.0039
783	1080	2100	14.60	0.1790	0.1790	35970	2.0000	0.0020
1273	1080	5750	11.70	0.1320	0.1320	35970	2.0000	0.0020
3589	1080	5875	10.00	0.1000	0.1000	35970	2.0000	0.0020
3640	1080	5875	10.00	0.1000	0.1000	1000	1.0000	0.0010

Those properties were measured up to the fiber sublimation temperature, 3589 K. Values beyond the fiber sublimation temperature were extrapolated. The critical sublimation temperature of pure solid carbon is 3640 K. At the critical sublimation temperature, the latent heat of vaporization ΔH_v is 4.3×10^4 kJ/kg. Lee *et al*. assumed that the CFRP was completely sublimated without residues when the temperature exceeded the critical sublimation temperature of solid carbon [19].

Many systems have been developed to protect an aircraft from lightning strokes. Among them, the copper expanded metal foil (EMF) developed by Dexmet Corporation as a LPS for the CFRP structure of aircraft was selected in the present work. Because the copper EMF is highly electrically conductive, it protects the CFRP layer by rapidly dispersing the charges caused by the lightning strike. The temperature-dependent properties of copper EMF should also be considered when performing a fully coupled thermal-electrical analysis. The EMF was assumed to be made up of pure copper isotropic properties [19]. The measured values of the properties of the copper EMF at various temperatures are tabulated in Table 5.

Table 5. Material properties of the copper EMF [19]

Temp., T (K)	Density, ρ (kg/m^3)	Specific Heat Cp (J/kg · K)	Thermal Conductivity, k (W/m·K)	Electrical Conductivity, σ (S/m)
298	8950	385	400	58140000
773	8950	431	370	20120000
783	8950	491	340	4651000
1273	8950	492	150	3704000

2873	8950	493	180	2227000
3500	8950	494	180	1500000
4773	8950	495	180	1470000
8273	8950	495	180	1400000

According to the data available, the melting point of pure copper is 1356 K and the boiling point is 2840 K. The critical thermodynamic temperature of pure copper is 8273 K. Both thermal and electrical conductivities at critical temperatures were calculated using a second-order extrapolation. The latent heat of melting ΔH_f of the copper EMF is 2.05×10^2 kJ/kg and the latent heat of vaporization ΔHv is 4.8×10^3 kJ/kg.

5.3 Initial and Boundary Conditions for Computational Simulation

The computational model of the upper spar cap of the main rotor blade was described in Section 5.1. The transverse dimensions and width of the specimen model were 100 mm and 100 mm, respectively. The total thickness of 0.5 mm was achieved by adding up four plies with a thickness of 0.125 mm [18]. The impulse current of the lightning strike was attached at the center of the top layer of the specimen. The point of exit where the lightning energy was emitted was set on the bottom and side of the specimen. The electrical potential at the sides and bottom is 0 V, which implies grounding. The initial conditions for the specimen were set at the ambient temperature condition of 298 K. Surface radiation conditions were imposed on the top layer where the strike point was located, and the thermal radiation emissivity of the surface was set at 0.9 [6,29,40]. Figure 5 shows the initial and boundary conditions of the present multiphysics computational simulation.

The energy source of the impulse current of the lightning had the component A waveform, corresponding to Zone 1A with a high probability of initial attachment. The definition and parameters of the waveform defined in IEC60060-1 standard are described in Fig. 6. T1 is the front time, and T2 is the time taken to reduce to reach 50% of the peak current. The peak current of the component A waveform can be up to 200 kA, but we selected 40 kA 4/20 waveforms, which is the level usually applied to lightning experiments on a laboratory scale [17,30]. The electrical charge Q of the simulated waveform was 0.49 C and action integral I was $11.5\times10^3 A^{2s}$. The electrical charge and action integral were defined as follows, respectively [40],

$$Q = \int_0^t i dt \tag{8}$$

$$I = \int_0^t i^2 dt \tag{9}$$

A local linear approximation shows the impulse current information at the time the waveform was input to ABAQUS for the computational analysis.

In this simulation, we employed a simplified model without considering the arc heating. According to a study by Wang *et al.* [22], the arc heating effect can affect the thermal damage area of a waveform having a long duration at a low amplitude, such as the current waveform C. However, in this study, the arc heating model was not included, since we focused on a short time and high amplitude lightning waveform A, which is very different from the waveform C.

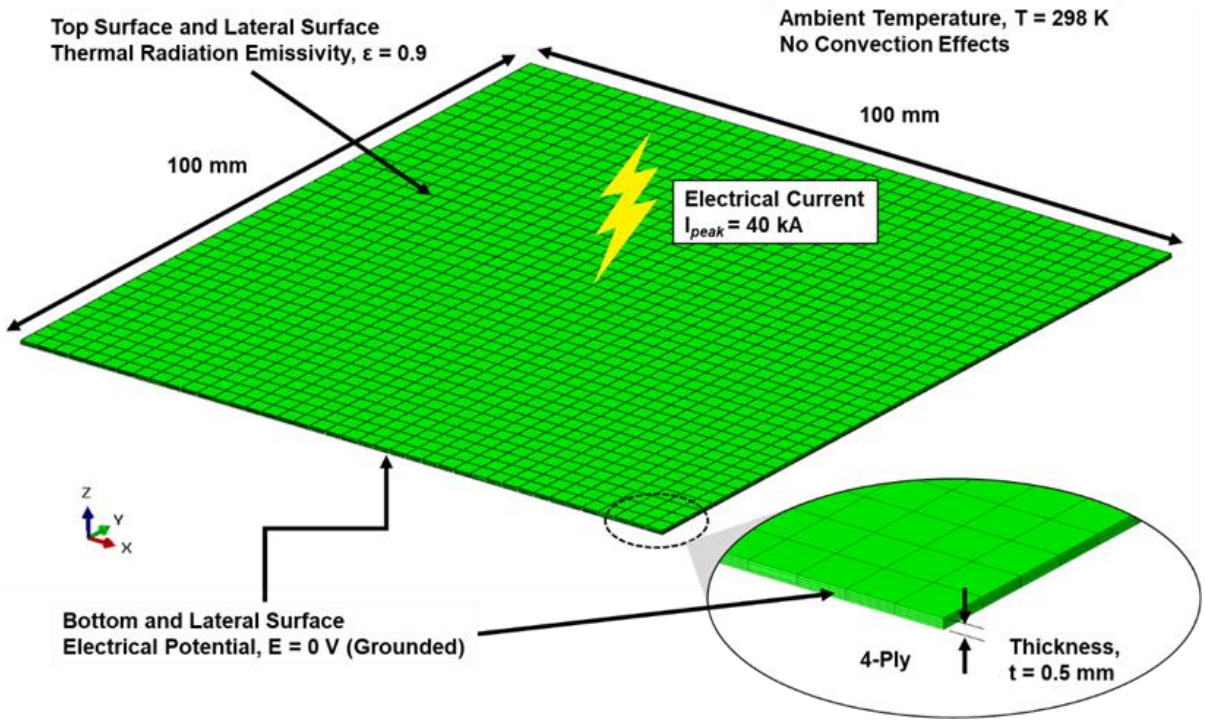

Figure 5. Initial and boundary conditions of coupled thermal-electrical specimen model for multiphysics analysis

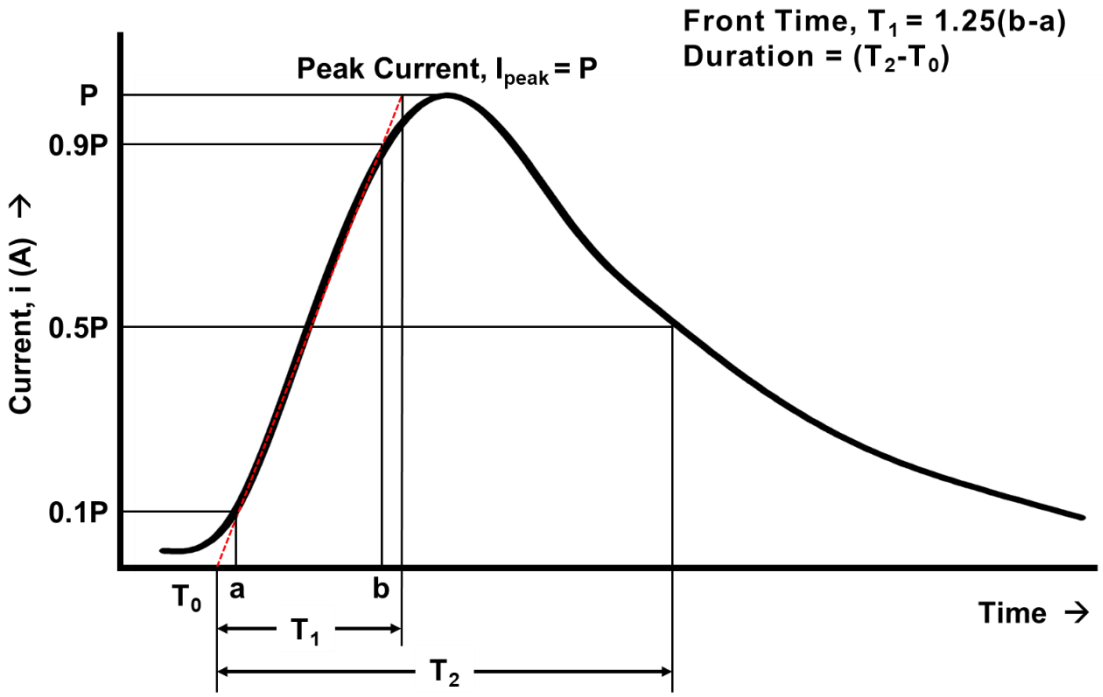

Figure 6. Definition of the parameters of the simulated waveform

6. Results and Discussion

6.1 Thermal and Electrical Response of CFRP Protected and Unprotected by EMF

CFRP lightning damage can be assessed by the temperature distribution of the NT11 (nodal temperature) solutions obtained with ABAQUS. The present analysis considers both a CFRP protected by EMF and the CFRP without any protection. Figure 7 shows the temperature distribution in the CFRP not protected by EMF. The area indicated by the contour lines depicts the temperature rise due to lightning. The scope of the CFRP damaged area is based on a reference temperature of a value 300 °C (573 K), at which the epoxy inside the composite begins to decompose. In particular, the cross-section at the center of the specimen shows a noticeable puncture along the thickness direction due to the lightning strike, and thermal damage due to sublimation of the CFRP in the fiber direction in the top layer.

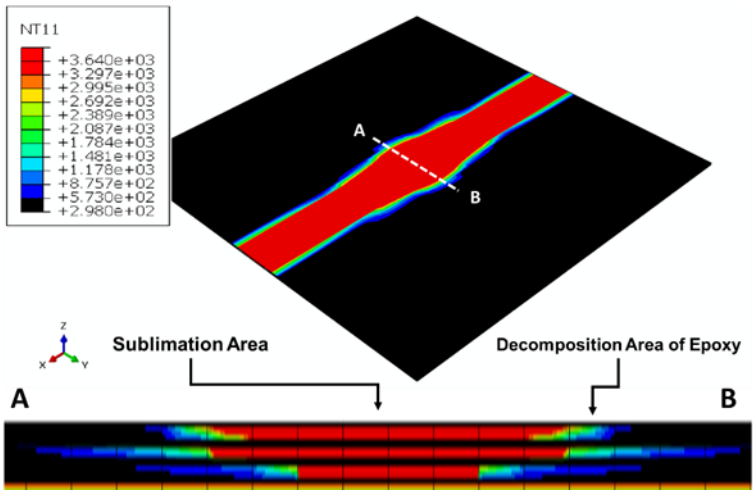

Figure 7. Distribution of thermally damaged area of the CFRP unprotected by EMF

Figure 7 further shows that the maximum temperature at the lightning attachment point increased to an unrealistic value of 1.078×10^{7} K, which can be attributed to the Joule heating effects. Beyond the critical temperature, the process of carbon sublimation initiates, when it can no longer sustain the Joule heating.

However, the present computational simulation considers only the latent heat of the material, without taking into account the effect of interlayer insulation due to the sublimation or separation of the materials occurring in the three-dimensional space. This causes a continuous transfer of heat and

electrical energy from the first layer to the next, resulting in the unrealistic maximum temperature value. Therefore, referring to previous studies by [17,19], the maximum surface temperature of CFRP was limited to not exceed the critical sublimation temperature of carbon (3640 K).

The model of the CFRP protected by EMF is shown in Fig. 8, where the copper EMF is placed on the top layer of the specimen. The actual geometry of the copper EMF used in the ABAQUS solver for computational analysis is shown in Fig. 8 [40].

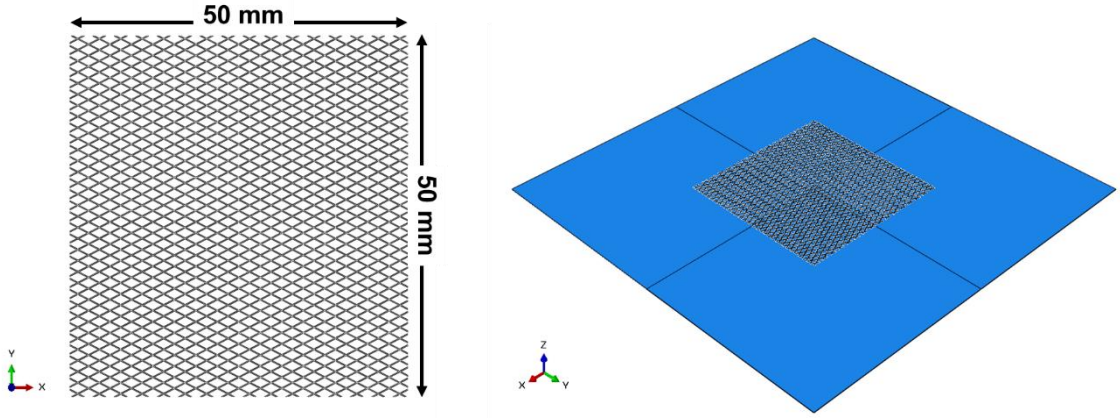

Figure 8. Computational model for the CFRP protected by the copper EMF

The contact characteristics of different materials, such as copper EMF and CFRP, must be included in order to perform the coupled thermal-electrical simulation in the model [2]. Incomplete contact between the copper EMF and CFRP can result in significant thermal and electrical resistance, since the copper EMF and CFRP have different electrical and thermal properties. In general, the contact properties are determined as a function of temperature and pressure at the boundary, and the surface roughness (gap).

The electrical contact properties are defined as follows [36],

$$
\begin{aligned}
J &= \sigma_g(\varphi_A - \varphi_B) \\
\sigma_g &= \sigma_g(\bar{\theta}, d, p, \bar{f}^{\alpha}) \\
\bar{\theta} &= \frac{1}{2}(\theta_A + \theta_B) \\
\bar{f}^{\alpha} &= \frac{1}{2}(f^{\alpha} + f^{\beta})
\end{aligned}
\tag{10}
$$

Here J is the current density passing through the interface at each of the points A and B on the two

contacting surfaces, φ_A and φ_B are the electrical potentials at points A and B, and σ_g is the electrical gap conductance. $\bar{\theta}$ is the average temperature at points A and B, and d, p are the gap clearance and pressure at the contact point, respectively. $\bar{f}^{\alpha}$ is the predefined electrical field parameter at points A and B.

Similarly, the thermal contact properties can be defined as follows [36],

$$\begin{aligned} q &= k(\theta_A - \theta_B) \\ k &= k(d, p, \bar{\theta}, \overline{|\dot{m}|}, \overline{f_\gamma}) \\ \bar{\theta} &= \frac{1}{2}(\theta_A + \theta_B) \\ \overline{f_\gamma} &= \frac{1}{2}(f_\gamma^A + f_\gamma^B) \end{aligned} \tag{11}$$

Here q is the heat flux per unit area passing through the interface at points A and B, k is the thermal gap conductance, $\overline{|\dot{m}|}$ is the average of the mass flow rate per unit area of the contact surface at A and B, and $\overline{f_\gamma}$ is a predefined thermal field variable. In this study, in order to avoid additional electrical and thermal resistance between EMF and CFRP, it is assumed that there is no gap, the pressure is constant, and the surfaces have perfect contact.

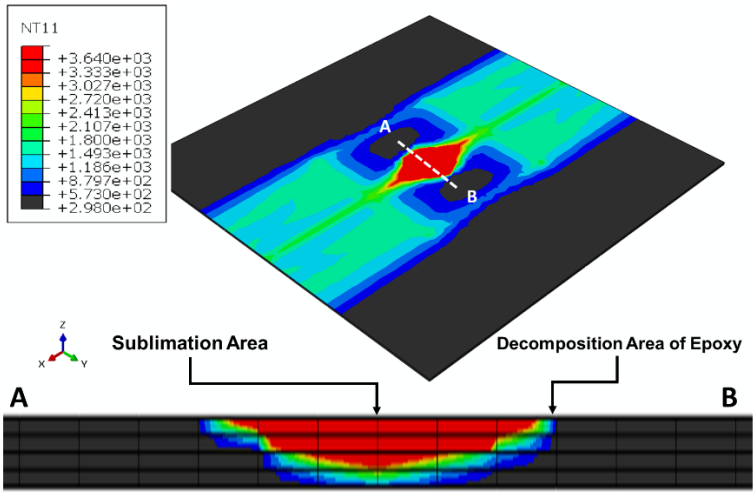

Figure 9. Distribution of thermally damaged area of the CFRP protected by the copper EMF

Figure 9 shows the results of the computational analysis of the CFRP specimens protected by the copper EMF under the lightning strike conditions. It shows that, unlike Fig. 7, the CFRP protected by the EMF layer did not suffer penetration failure due to sublimation [6]. Additionally, the

decomposition area of the epoxy along the fiber direction increased in the top layer. This was due to the Joule heating effect, caused by the electrical-thermal conductivity, which changes rapidly as the current flowing through the EMF passes through the CFRP at the end of the EMF [21].

Figure 10 provides snapshots of a fracture zone in each layer caused by the sublimation of carbon. It can be seen that the damaged area in the CFRP protected by the EMF as a whole has been significantly reduced because of carbon sublimation. When the computational results were compared with data obtained from the lightning test of the CFRP protected by the EMF, it was evident that the distribution of fracture zones in the top layer matched each other well, as shown in Fig. 11 [5,15].

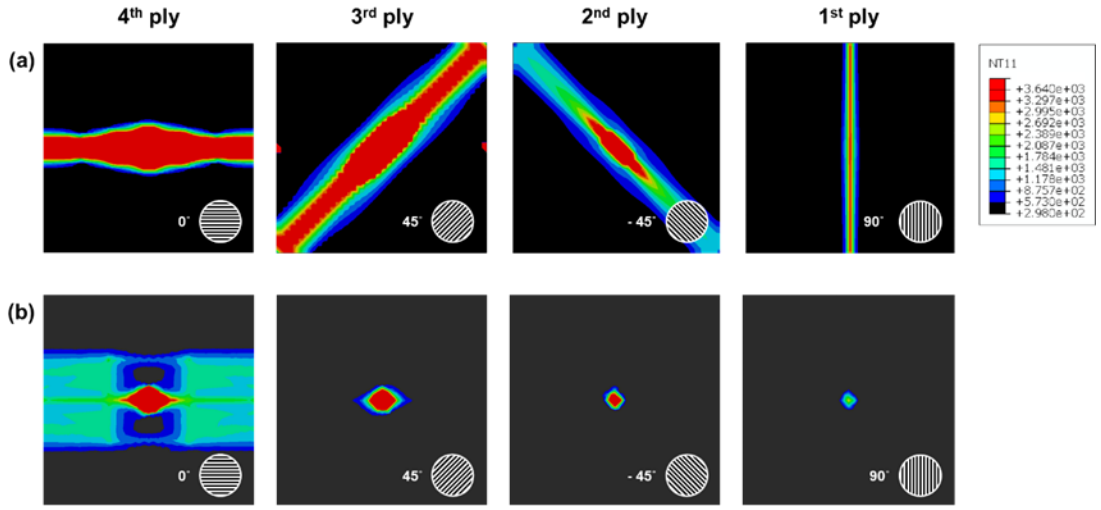

Figure 10. Thermally damaged region by sublimation: (a) unprotected, (b) protected by EMF

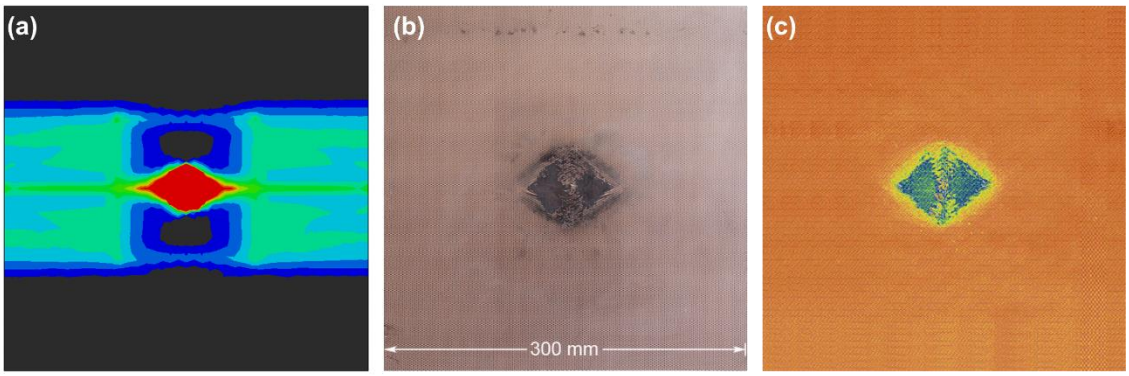

Figure 11. Comparison of computational simulation and experimental results for the CFRP protected by EMF: (a) computational simulation result, (b) experimental result [15], (c) ultrasonic C-scan of specimen [15]

Figure 12 shows the extent of the area of copper damaged by melting and vaporization. The area under the vaporization zone was completely vaporized when the temperature exceeded the critical temperature of copper, while the material in the melting zone was not entirely vaporized, and there was a possibility that residue remained. According to Guo *et al.* [15], the geometric shape of EMF can affect the electrical conductivity as an anisotropic material. Therefore, the damage area of the EMF through lightning strike test and simulation appeared as an ellipse or diamond.

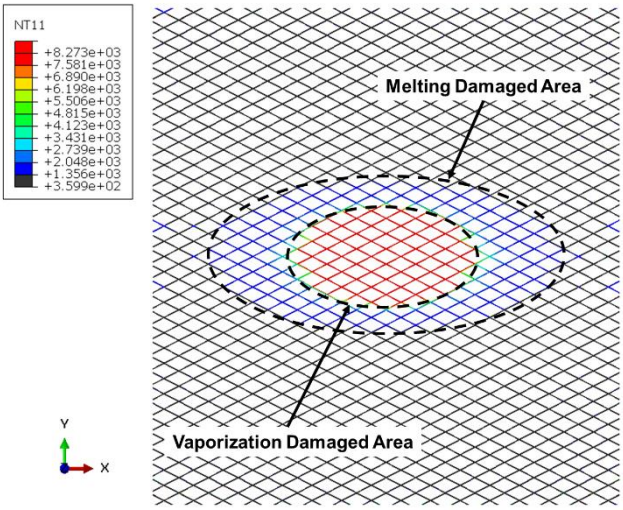

Figure 12. Vaporization and melting area according to the temperature profile of the copper EMF

Using these results, the rate of material ablation can be estimated numerically based on the vaporization of the lightning protection layer. The Hertz-Knudsen model computes the ablation rate (defined by the vaporization progress distance per unit time of the material) as a function of the temperature. The ablation rate can then be expressed as [19,40],

$$\nu(T) = (1-\beta)\sqrt{\frac{m}{2\pi k_B T}\frac{p_0}{\rho}}\exp\left[\frac{L_v}{k_B}\left(\frac{1}{T_{BT}}-\frac{1}{T}\right)\right] \tag{12}$$

Here β is the sticking coefficient, k_B is the Boltzmann constant, L_v is the latent heat of vaporization, T_{BT} is the boiling temperature at 1 atm (p_0), and m is the molar mass of the material. For the copper material, this reduces to

$$\nu(T)_{CM} = \frac{0.395}{\sqrt{T}}\exp\left(3.696\times10^4\left(\frac{1}{2840}-\frac{1}{T}\right)\right) \tag{13}$$

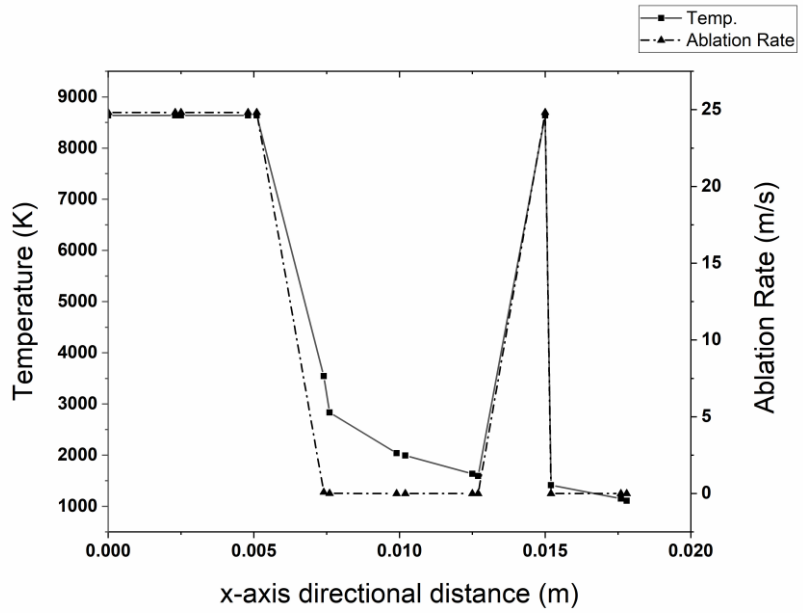

Figure 13. Ablation rate and temperature distribution along the *x*-axis direction

The ablation rate from this calculation and the temperature are shown along the *x*-axis direction from the center of the EMF in Fig. 13. The variation in ablation rate and the variation in temperature have generally similar forms [41]. However, there is a difference between the temperature and the ablation rate, at the location where the temperature is less than the boiling temperature of copper (2840 K). Towards the end of the EMF, the temperature and the ablation rate increase, due to rapid changes in electrical resistance at the point of contact between the EMF and CFRP [40].

6.2 Thermal and Electrical Response of Curved CFRP

We also consider a curved CFRP specimen with a two-dimensional curvature observed in the cross section of a main rotor blade. The cross section of the rotor blade is an airfoil shape and is composed of curved surfaces having various curvatures depending on each point. In Figure 3, the upper spar cap and leading edge have small and large curvature, respectively. Therefore, to analyze the simulation according to the lightning attachment point of the main rotor blade, a cylindrical CFRP composite specimen with various curvatures was modeled as shown in Fig. 14.

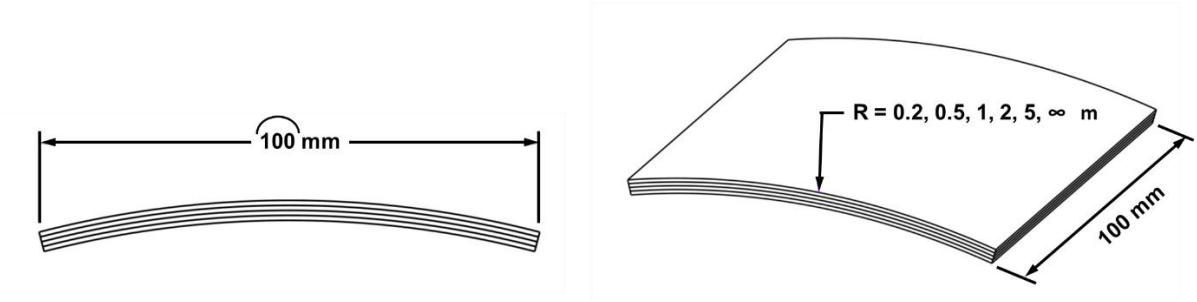

Figure 14 Configuration of cylindrical multilayered CFRP model

The simulation was performed with the same initial and boundary conditions as the composite plate model in Fig. 5. In Figure 15, it can be seen that the 4th layer has little or no variation in the thermal damage area due to curvature. For the flat plate CFRP model with infinite curvature, the distribution of the thermal damage area is formed along the fiber orientation of the composite layer. On the other hand, it can be seen that the thermal damage area of the curved CFRP model follows less carbon fiber orientation than the plate model. This tendency is noticeable as the curvature increases (as the radius of curvature decreases).

The area of thermal damage was evaluated by the number of mesh elements. Figure 16 shows the number of elements corresponding to the total thermal damage area, including sublimation and decomposition, for different curvatures. The third layer tends to increase the number of thermal damage elements as the curvature increases. For the second layer, it can be seen that the number of thermal damage elements increases as the curvature increases except for R = 5 m and the flat plate model. The R = 5 m model seems to deviate from the overall trend but shows the intermediate behavior between the flat plate model and the R = 2 m model.

Finally, Fig. 17 shows the number of sublimation elements according to the change in curvature. Sublimation occurs extensively in the third layer for the entire curved model except for the plate model. The sublimated element of the third layer increases as the curvature increases, and then start to decrease at a radius of curvature of R = 1 m. The number of sublimation elements in the third layer represents the intensity of the effect on other layers. When the heat energy absorbed by sublimation increases in the third layer, the number of thermal damage elements due to sublimation in the first and second layers decreases.

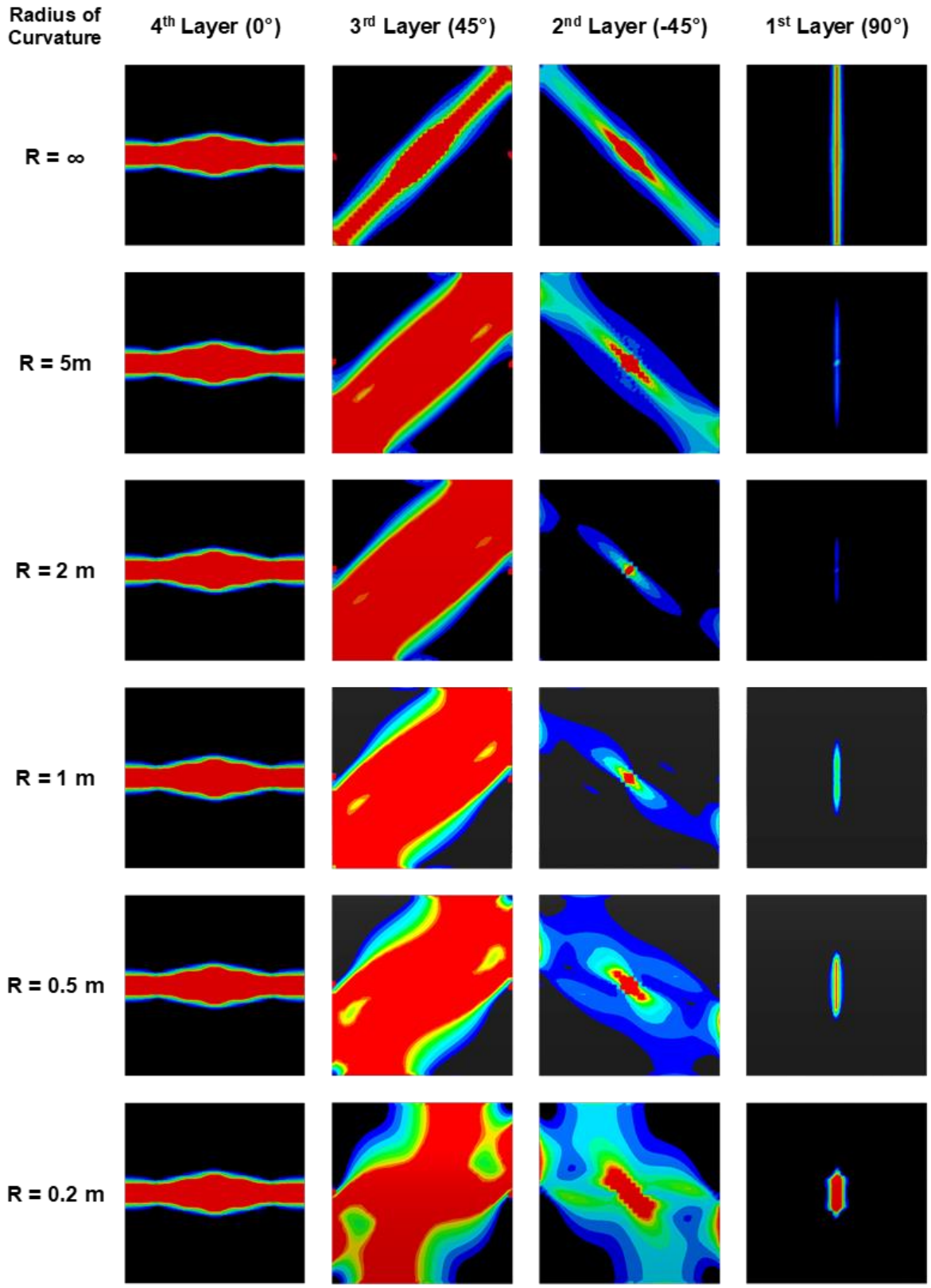

Figure 15. Distribution of thermally damaged area depending on the radius of curvature

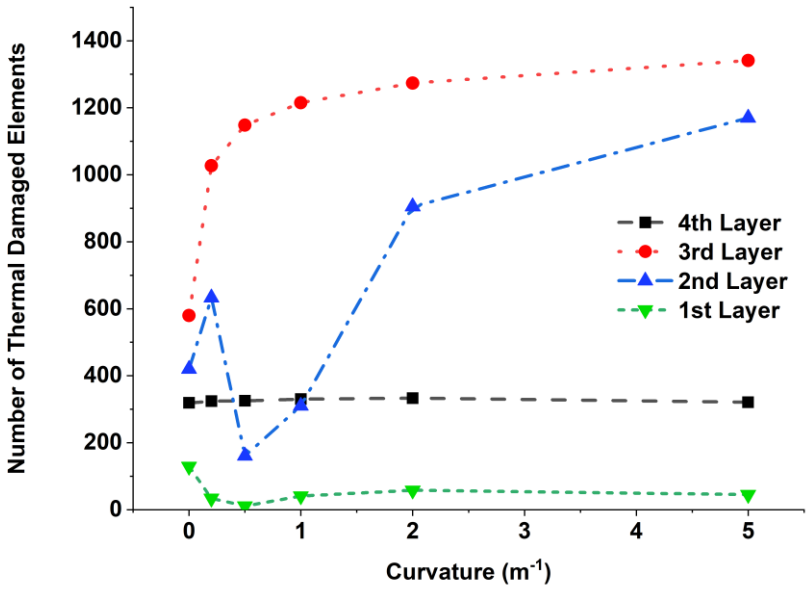

Figure 16. Number of thermal damaged elements (sublimation and decomposition)

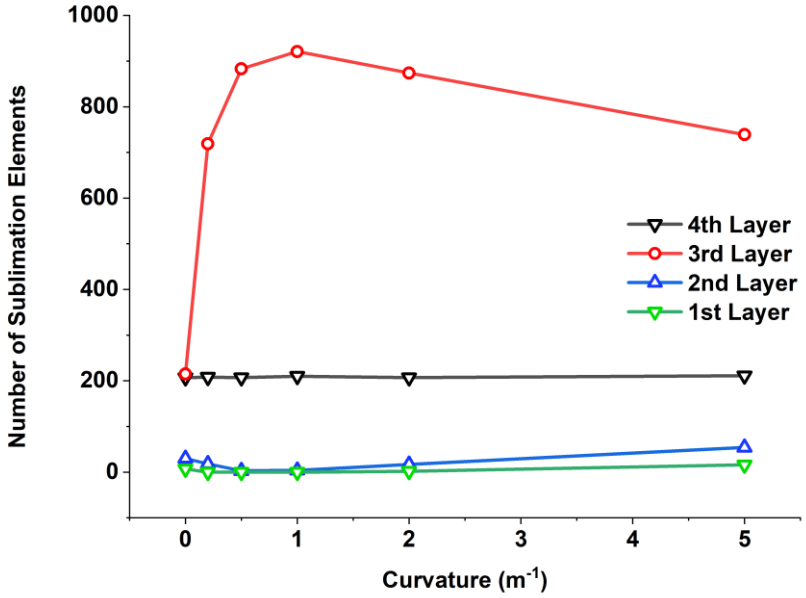

Figure 17. Number of thermal damaged elements (sublimation only)

6.3 Estimation of Lightning Damaged Area for Different Geometric Parameters of EMF

Depending upon the choice of raw materials and geometric parameters, it is possible to develop several types of EMF with varying performance. In particular, the geometric parameters change the ratio of the coverage area (open area) of the EMF, which in turn changes the weight and electrical

characteristics [20]. The present study considers several different cases with varying geometric parameters and investigates the effects of the geometric parameters on the performance of the copper EMF.

Figure 18 shows the geometric parameters of the EMF, including the long way of diamond (LWD), short way of diamond (SWD), and strand width (SW). The geometrical details of the six cases considered in this study are tabulated in Table 6. Cases I, II, and III are classified according to the changes in LWD and SWD, while cases 1 and 2 are classified according to the changes in the strand width of EMF. Figure 19 shows examples of the EMF with different geometric parameters. As LWD and SWD increase, the open area increases.

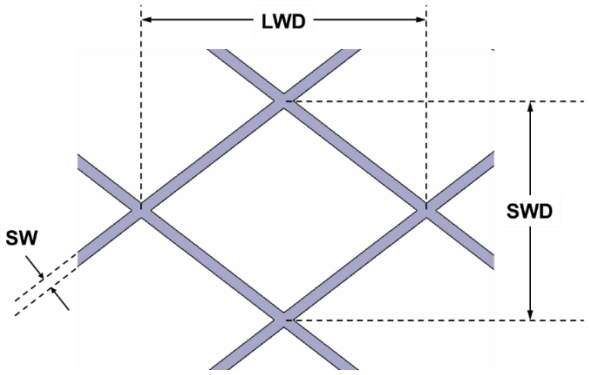

Figure 18. Geometric parameters of the EMF [5,15]

Table 6. Cases according to the EMF geometric parameters

Case		Code	LWD (mm)	SWD (mm)	SW (mm)	Thickness (mm)
EMF 1	I	2CU4-100	2.5400	1.4846	0.1016	0.0508
	II	2CU4-180	4.5720	2.3178	0.1016	0.0508
	III	2CU4-250	6.3500	3.3871	0.1016	0.0508
EMF 2	I	2CU8-100	2.5400	1.4846	0.2032	0.0508
	II	2CU8-180	4.5720	2.3178	0.2032	0.0508
	III	2CU8-250	6.3500	3.3871	0.2032	0.0508

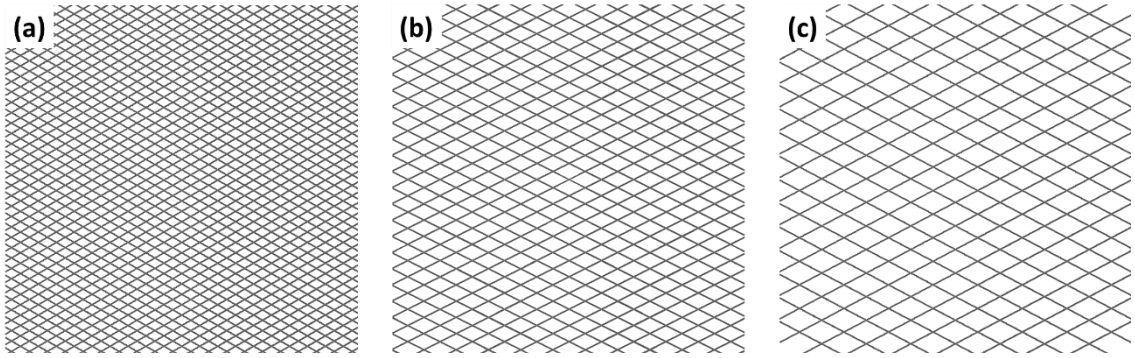

Figure 19. Examples of the EMF with different geometric parameters: (a) case 2-I, (b) case 2-II, (c) case 2-III

Figure 20 shows the EMF vaporized area according to different design parameters. As expected, the design parameters LWD, SWD, and SW significantly affected the area vaporized by lightning. The vaporization area of the EMF increased with increases in LWD and SWD, but with a decrease in SW. The changes in LWD, SWD, and SW resulted in a change in the open area per unit area. As the open area increased, and as the SW decreased, the electrical conductivity per unit area of the EMF decreased. The increase in electrical resistance interferes with the rapid dispersion of lightning current energy and thus increases the temperature due to the Joule heating effect, ultimately causing more significant thermal damage to the CFRP layers located under the EMF.

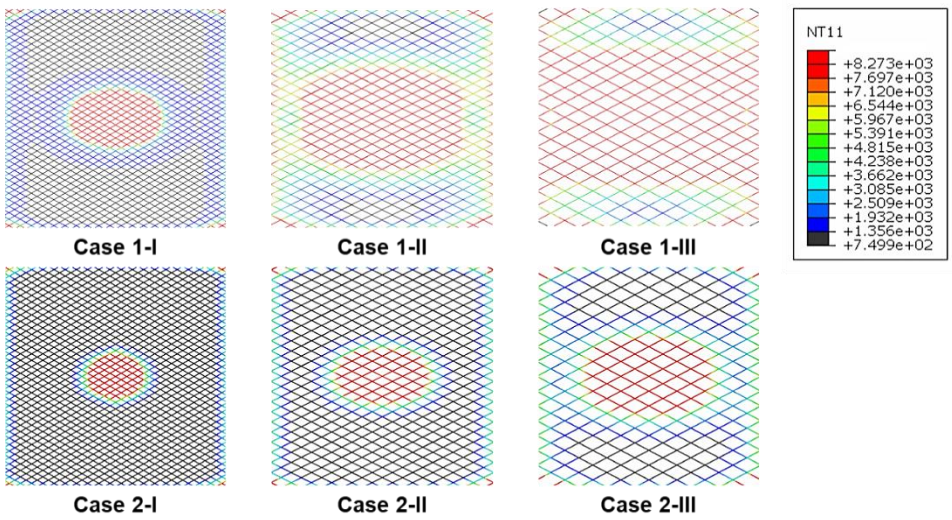

Figure 20. Distribution of the EMF vaporization area

Figures 21 to 23 show a comparison of temperature distribution at the center of the specimen (the point of lightning attachment) in the depth direction. A comparison of the temperature distribution at different LWD and SWD in cases 1 and 2 are shown in Figs. 21 and 22, respectively. In both cases, as the open area of EMF increases, the temperature in the depth direction increases and the temperature of the bottom layer at the exit point of the lightning current also increases [15].

Figure 23 shows the effect of the strand width by comparing the temperatures of two cases, 1-I and 2-I. It can be seen that the temperature decreases more rapidly when SW increases at constant LWD and SWD. The temperature difference at the bottom layer was shown to be 241 K. Since the maximum temperature difference between case 1-III and case 2-III was found to be 383 K from Figs. 21 and 22, it is obvious that reducing LWD and SWD while increasing SW improves the lightning protection performance of the copper EMF. However, this scheme can also result in a considerable increase in the weight of the structures. Therefore, the geometric parameters of the EMF such as LWD, SWD, and SW should be carefully chosen by considering the zoning, peak currents, and penalties.

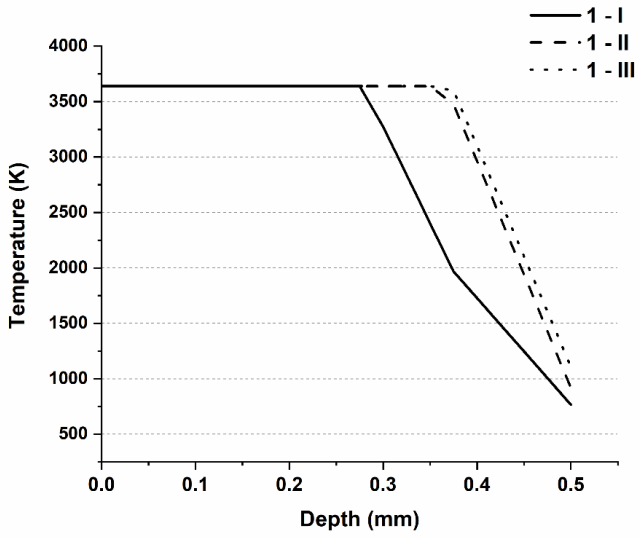

Figure 21. Temperature profiles along the depth of the composite for case 1 according to opening rate

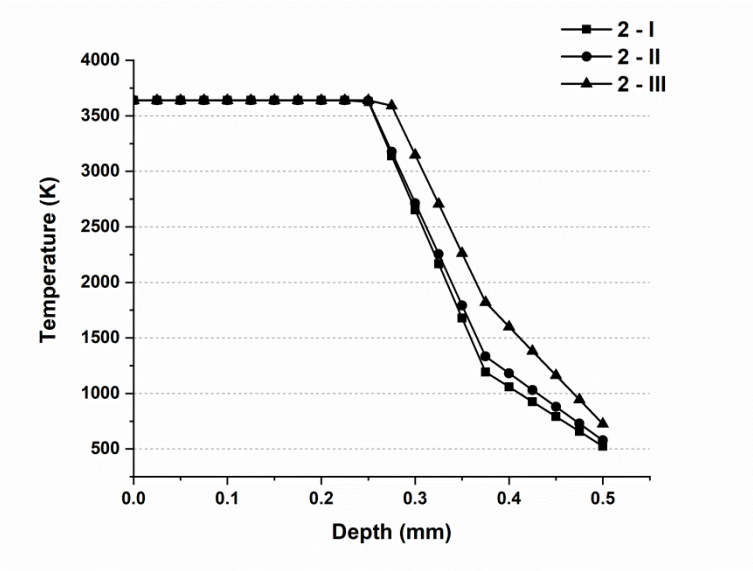

Figure 22. Temperature profiles along the depth of the composite for case 2 according to opening rate

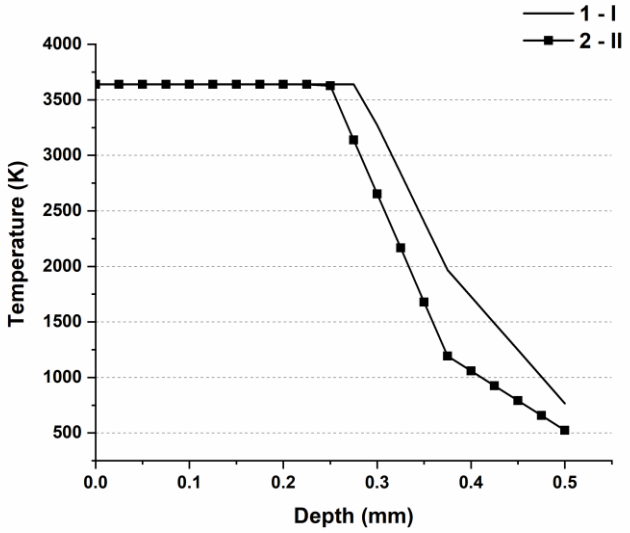

Figure 23. Comparison of temperature profiles for cases 1 and 2

7. Conclusion

We carried out a multiphysics computational simulation of the effects of lightning strikes on the CFRP rotor blade, one of the major components in the lightning certification of rotorcraft. The lightning waveform implemented in the computational simulation was consistent with the lightning certification regulations and guidance for rotorcraft. The anisotropic properties of materials such as the CFRP were considered to improve the accuracy of the simulation. The changes in the properties of a material caused by heat generated during lightning strikes were also modeled in order to match

those observed in an actual lightning test. We employed a simplified model without considering the arc heating, since our main focus was placed on a short time and high amplitude lightning waveform. However, when responses to various waveforms caused by various lightning conditions are main concern, the arc heating effect must be considered.

We also conducted a computational analysis to verify the effectiveness of a lightning protection system, a copper EMF. The sublimation area of the CFRP was evaluated based on the temperature distribution in the CFRP with and without EMF. In the model without EMF, sublimation failure occurred in the top layer of the CFRP fibers in the longitudinal direction, while sublimation failure occurred in the other four layers along the thickness direction. On the other hand, in the model with EMF, no sublimation was observed in the longitudinal direction. Moreover, the sublimation failure did not proceed to the bottom layer along the lateral direction. In addition, we showed that the geometric parameters of the EMF have a significant effect on its protection performance against lightning strike. By investigating a total of six cases with different design parameters, it was found that EMF performance improves as the open area of the EMF increases, and the strand width composing the EMF grid increases. The reason is that the geometric parameters of the EMF change the electrical conductivity and resistance, which is closely related to the lightning protection performance. However, as EMF protection performance increases, the weight of the CFRP may also increase. Therefore, when designing the lightning protection system using EMF, it is important to consider not only the peak current characteristics of the various lightning zoning, but also penalties.

In this study, the effect on the composite material of the main rotor blades of a rotorcraft was analyzed in a specimen unit. The scope of research has been extended from simulations for flat plate model to simulations of curved model. Based on the simulation results, a correlation between curvature and thermal damage area was obtained. This work can contribute to the prediction of the thermal damage area for aircraft components composed of composite materials with various curvatures, such as rotor blades. These case studies can also provide more detailed information in the factors considered for optimization of the lightning protection system and contribute to improving the certification process. In addition, it will remain essential to validate the simulation results of curved

composites using actual experimental data as a future work.

Acknowledgments

This work was supported by the Korea Institute of Aviation Safety Technology (KIAST) Grant funded by the Ministry of Land, Infrastructure and Transport (19CHTR-C128889-03), South Korea.

References

1. Wilkinson JM, Wells H, Field PR (2013) Investigation and prediction of helicopter-triggered lightning over the North Sea. Meteorological Applications 20(1):94-106
2. Chemartin L, Lalande P, Peyrou B, Chazottes A, Elias PQ, Delalondre C, Cheron BG, Lago F (2012) Direct effects of lightning on aircraft structure: analysis of the thermal, electrical and mechanical constraints. Aerospacelab:1-15
3. Han SH (2005) Certification of aircraft system and avionics equipment against lightning indirect effect. Aerospace Engineering and Technology 4(1):248-259
4. Fisher F, Plumer JA, Perala, RA (1989) Aircraft lightning protection handbook. Lightning Technologies Inc., Pittsfield, MA, ADA222716
5. Gagné M, Therriault D (2014) Lightning strike protection of composites. Progress in Aerospace Sciences 64:1-16
6. Kim JJ, Baek ST, Song DG, Myong RS (2016) Computational simulation of lightning strike on aircraft and design of lightning protection system. Journal of the Korean Society for Aeronautical & Space Sciences 44(12):1071-1086
7. Lalande P, Bondiou-Clergerie A, Laroche P (1999) Computations of the initial discharge initiation zones on aircraft or helicopter. 1999 International Conference on Lightning and Static Electricity (ICOLSE), Society of Automotive Engineers, Warrendale, PA
8. Jeong DY, Yang HD (2016) A study on the direct effect of lightning on structures and systems of aircraft. Journal of Aerospace System Engineering 10(2):41-45
9. Jeong DY, Yang HD (2017) A study on lightning test of main rotor blade. The Society for Aerospace System Engineering:92-94

10. Guo Y, Xu Y, Wang Q, Dong Q, Yi Z, Jia Y (2019) Eliminating lightning strike damage to carbon fiber composite structures in Zone 2 of aircraft by NI-coated carbon fiber nonwoven veils. Composites Science and Technology 169:95-102
11. Zhang J, Zhang X, Cheng X, Hei Y, Xing L, Li Z (2019) Lightning strike damage on the composite laminates with carbon nanotube films: Protection effect and damage mechanism. Composite Part B 168:342-352
12. Chu H, Xia Q, Zhang Z, Liu Y, Leng J (2018) Sesame-cookie topography silver nanoparticles modified carbon nanotube paper for enhancing lightning strike protection. Carbon: https://doi.org/10.1016/j.carbon.2018.11.022
13. Alemour B, Badran O, Hassan M R (2019) A review of using conductive composite materials in solving lightning strike and ice accumulation problems in aviation. Journal of Aerospace Technology and Management 11: e1919. https://doi.org/10.5028/jatm.v11.1022.
14. Hu T, Yu X (2019) Lightning performance of copper-mesh clad composite panels: Test and simulation. Coatings 9(11):727. https://doi:10.3390/coatings9110727
15. Guo Y, Xu Y, Zhang L, Wei X, Dong Q, Yi X, Jia Y (2019) Implementation of fiberglass in carbon fiber composites as an isolation layer that enhances lightning strike protection. Composite Science and Technology 174:117-124
16. Guo Y, Xu Y, Wang Q, Dong Q, Yi X, Jia Y (2019) Enhanced lightning strike protection of carbon fiber composites using expanded foils with anisotropic electrical conductivity. Composites Part A: Applied Science and Manufacturing 117:211-218
17. Wang FS, Zhang Y, Ma XT, Wei Z, Gao JF (2019) Lightning ablation suppression of aircraft carbon/epoxy composite laminates by metal mesh. Journal of Materials Science & Technology 35:2693-2704
18. Ogasawara T, Hirano Y, Yoshimura A (2010) Coupled thermal–electrical analysis for carbon fiber/epoxy composites exposed to simulated lightning current. Composites Part A: Applied Science and Manufacturing 41(8):973-981

19. Ranjith R, Myong RS, Lee SW (2014) Computational investigation of lightning strike effects on aircraft components. International Journal of Aeronautical and Space Sciences 15(1):44-53
20. Lee J, Lacy Jr TE, Pittman Jr CU, Mazzola MS (2018) Thermal response of carbon fiber epoxy laminates with metallic and nonmetallic protection layers to simulated lightning currents. Polymer Composites 39(S4):E2149-E2166
21. Morgan J (2013) Thermal simulation and testing of expanded metal foils used for lightning protection of composite aircraft structures. SAE International Journal of Aerospace 6(2):371-377
22. Wang FS, Yu XS, Jia SQ, Li P (2018) Experimental and numerical study on residual strength of aircraft carbon/epoxy composite after lightning strike. Aerospace Science and Technology 75:304-314
23. Chen H, Wang FS, Ma XT, Yue ZF (2018) The coupling mechanism and damage prediction of carbon fiber/epoxy composites exposed to lightning current. Composite Structures 203:436-445
24. Wang F, Ma X, Zhang Y, Jia S (2018) Lightning damage testing of aircraft composite-reinforced panels and its metal protection structures. Applied Sciences 8(10):1791-1801
25. Wan G, Dong Q, Zhi J, Guo Y, Yi X, Jia Y (2019) Analysis on electrical and thermal conduction of carbon fiber composites under lightning based on electrical-thermal-chemical coupling and arc heating models. Composite Structures 229: 111486
26. Wang Y, Zhupanska OI (2015) Lightning strike thermal damage model for glass fiber reinforced polymer matrix composites and its application to wind turbine blades. Composite Structures 132: 1182-1191
27. Millen SLJ, Murphy A, Abdelal G, Catalanotti G (2019) Sequential finite element modelling of lightning arc plasma and composite specimen thermal-electric damage. Computers and Structures 222:48-62
28. Xiao Y, Yin J, Li S, Yao X, Chang F (2018) Characterization of composite laminate lightning strike thermal-mechanical coupling damage based on progressive damage Model. 7th International Conference on Energy, Environment and Sustainable Development (ICEESD 2018)
29. Foster P, Abdelal G, Murphy A (2019) Quantifying the influence of lightning strike pressure loading on composite specimen damage. Applied Composite Materials 26(1):115-137

30. Karch C, Arteiro A, Camanho PP (2019) Modelling mechanical lightning loads in carbon Þbre-reinforced polymers. International Journal of Solids and Structures 162:217-243
31. Millen SLJ, Murphy A, Catalanotti G, Abdelal G (2019) Coupled thermal-mechanical progressive damage model with strain and heating rate effects for lightning strike damage assessment. Applied Composite Materials 26(5-6):1437-1459
32. Nunes de Souza LF (2007) Modeling of direct effects of lightning on composite structures of aircraft. 2007 International Conference on Lightning and Static Electricity (ICOLSE), PPR59, Paris, 2007
33. Espejel JFT, Khodaei ZS (2017) Lightning strike simulation in composite structures. Key Engineering Materials 754:181-184
34. Rupke E (2002) Lightning direct effects handbook. Lightning Technologies Inc., AGATE-WP3.1-031027-043-Design Guideline, Pittsfield, MA
35. Morgan D, Hardwick CJ, Haigh SJ, Meakins AJ (2012) The interaction of lightning with aircraft and the challenges of lightning testing. Aerospacelab:1-10
36. Dassault Systémes Simulia Corp. Abaqus 6.14 analysis user's guide. Online Documentation. https://www.sharcnet.ca/Software/Abaqus/6.14.2/v6.14/books/usb/default.htm. Accessed 31 May 2019
37. Kumar D (2013) Design and analysis of composite rotor blades for active/passive vibration reduction. Doctoral Dissertation, University of Michigan, US
38. Rohl P, Dorman P, Sutton M, Kumar D, Cesnik CES (2012) A multidisciplinary design environment for composite rotor blades. 53rd AIAA/ASME/ASCE/AHS/ASC Structures, Structural Dynamics and Materials Conference 20th AIAA/ASME/AHS Adaptive Structures Conference 14th AIAA:1842
39. Bousman, WG (2003) Aerodynamic characteristics of SC1095 and SC1094 R8 airfoils. NASA/TP–2003-212265
40. Abdelal G, Murphy A (2014) Nonlinear numerical modelling of lightning strike effect on composite panels with temperature dependent material properties. Composite Structures 109:268-278

41. Lee SH, Park GS, Kim JG, Park JG (2019) Evaluation system for ablative material in a high-temperature torch. International Journal of Aeronautical and Space Sciences. https://doi.org/10.1007/s42405-019-00185-2